IEEE Access
Multidisciplinary | Rapid Review | Open Access Journal

Received February 13, 2020, accepted February 25, 2020, date of publication February 28, 2020, date of current version March 11, 2020.

Digital Object Identifier 10.1109/ACCESS.2020.2977299

Remote Sensing Image Fusion via Boundary Measured Dual-Channel PCNN in Multi-Scale Morphological Gradient Domain

WEI TAN[1,2], PEI XIANG[1], JIAJIA ZHANG[1], HUIXIN ZHOU[1], AND HANLIN QIN[1]

[1]School of Physics and Optoelectronic Engineering, Xidian University, Xi'an 710071, China
[2]Department of Computer Science, University of Copenhagen, 2100 Copenhagen, Denmark

Corresponding author: Wei Tan (twtanwei1992@163.com)

This work was supported in part by the National Natural Science Foundation of China under Grant 61675160, in part by the 111 Project under Grant B17035, and in part by the China Scholarship Council under Grant CSC201906960047.

ABSTRACT In this paper, a remote sensing image fusion method based on boundary measured dual-channel pulse-coupled neural network (PCNN) in multi-scale morphological gradient (MSMG) domain is proposed. Firstly, the panchromatic (PAN) image is decomposed into three parts, a small-scale image, a large-scale image, and a base image through a co-occurrence filtering (CoF)-based decomposition model. Secondly, an HSI transform is applied in the multispectral (MS) image to obtained intensity, hue and saturation components. Thirdly, a PCNN fusion strategy modulated by MSMG is used to fuse the base image and the intensity component of the MS image. Then, a fused intensity image is obtained by combining the small-scale image, large-scale image and the fused approximate image. Finally, the final fused image can be reconstructed by an inverse HSI transform. Experiments in four datasets demonstrate that the proposed method obtains the best performance in most cases.

INDEX TERMS Remote sensing image fusion, co-occurrence filtering, multi-scale morphological gradient, pulse-coupled neural network.

I. INTRODUCTION

Nowadays, with the rapid development of remote sensing technology, there are more types of remote sensing images are available when imaging a view [1], [2]. As a widely used remote sensing image, multispectral (MS) images containing plentiful spectral information are applied in the fields of disaster monitoring [3], marine research [4], object recognition [5], etc. However, the disadvantage of low spatial resolution makes it look blurry. The characteristic of a panchromatic (PAN) image is just the opposite of an MS image, which has high spatial resolution and low spectral resolution. Remote sensing images obtained from a single sensor have the disadvantage of incomplete information. Therefore, the MS and PAN image fusion (also called pansharpening) technology is crucial for obtaining an integrated image which contains plenty of spatial and spectral information.

In the past few decades, MS and PAN image fusion technology developed very rapidly. This technology is mainly divided into two categories: component substitution (CS) based algorithms [6]–[9] and multi-scale decomposition (MSD) based algorithms [10]–[14]. For the CS based algorithm, the MS images are decomposed into different transform domain, such as color/intensity space or principal components. Then the color/intensity spaces or first principal components are substituted by the corresponding contents of the PAN image. Finally, the fused image is reconstructed through the corresponding inverse transform. Classical CS based algorithms contains hue saturation intensity (HSI) transform [6], principal component analysis (PCA) [7], Gram-Schmidt (GS) [9], etc. The framework of these algorithms is very simple and can achieve efficient fusion performance in spatial resolution. However, since the bandwidth of PAN image cannot be completely covered by the MS images, some spectral distortions may occur.

Compared with the CS based algorithms, MSD based algorithms developed very rapidly. Famous MSD algorithms include: wavelet transform [10], curvelet transform [12], contourlet transform [13] and shearlet transform (NSST) [14]. In this kind of algorithms, the source images are first

The associate editor coordinating the review of this manuscript and approving it for publication was Haiyong Zheng.

decomposed into different scales of sub-images through corresponding MSD methods. Then the sub-images are merged based on different fusion rules in different sub-bands. Finally, an inverse MSD transform is used to reconstruct the fused image. The MSD based algorithms can achieve better performance in spectral domain. However, the spatial resolution of MSD based algorithms is lower than that of the CS based algorithms.

In recent years, edge-preserving filtering (EPF) algorithms have achieved good progress in image fusion field. The EPF has the characteristics of maintaining the edge structure. Meanwhile, some fine edges will be smoothed off [15]. According to this feature, a novel hybrid decomposition model is produced [16]–[18]. An EPF and Gaussian filtering (GF) is used in this model. Using the edge-preserving characteristic of EPF and the smoothing characteristic of GF, the input image is decomposed into three layers: small-scale layer, large-scale layer, and base layer. Classical EPF-GF decomposition methods include Bilateral-Gaussian filtering decomposition (BGFD) [16], Rolling guidance-Gaussian filtering decomposition (CGGFD) [17], and Curvature-Gaussian filtering decomposition (CGFD) [18]. This hybrid decomposition model has obtained great success in image fusion. Therefore, this type of method is an important branch of future image fusion research.

Inspired by the advantages of EPF, Jevnisek and Avidan proposed a novel EPF called co-occurrence filtering (CoF) [19]. Its biggest advantage is that the sharp details in a local region can be preserved when smoothing the fine textures. Since this characteristic, the edges within a local region can be preserved while the image is smoothed.

Over the past few years, neural networks have been widely used in many fields [20], [21]. As a method of stimulating the visual principle structure of cats, pulse-coupled neural network (PCNN) is a simplified neural network model. However, since one pixel corresponds to one neuron in the PCNN model, human eyes are not sensitive to edge information when using PCNN alone. Therefore, it is necessary to utilize a feature operation before the PCNN processing. The most commonly used feature operation is spatial frequency (SF) [22]. However, local block effect and blurring exist in the fused images, for the reason of inappropriate weighted coefficients of the sub-bands fusion.

In order to overcome the disadvantages, an effective remote sensing image fusion via CoF and multi-scale morphological gradient domain dual-channel PCNN is proposed in this paper. Firstly, the PAN image is decomposed into small-scale image, large-scale image and base image through a CoF and a GF. Secondly, an HSI transform is applied in the MS image to obtain intensity, hue and saturation components. Thirdly, the base image and the intensity component of MS image are merged in the light of multi-scale morphological gradient (MSMG) dual-channel PCNN fusion rule to obtain a fused approximate image. Then, combining the small-scale image, large-scale image and the fused approximate image to obtain a fused intensity image. Finally, the fused image can be reconstructed by an inverse HSI transform. Experimental results demonstrate that the proposed algorithm outperforms many state-of-the-art algorithms.

The main contributions of this proposed algorithm are as follows:

(1) The effective edge-preserving method CoF is first employed in the field of remote sensing image fusion. And the CoF-based image decomposition model is also presented in this paper.

(2) An effective sub-image fusion rule based on MSMG dual-channel PCNN (MSMG-PCNN) model is employed in this paper. The gradient information of the image can be easily extracted, and the size of structure can be easily changed to adapt to the scale of structure.

(3) The proposed CoF-MSMG-PCNN achieves the best performance in most cases in qualitative and quantitative.

The rest of this paper is organized as follows. The proposed algorithm which contains the theory of CoF and MSMG-PCNN is described in Section II. The experimental results are given in Section III, and the parameter discussion is given in Section IV. Finally, the conclusion is drawn in Section V.

II. PROPOSED METHOD

Remote sensing image fusion aims to produce an integrated image which contains plenty of spatial and spectral information. To realize the target, an effective remote sensing image fusion algorithm through CoF and MSMG-PCNN (we call it CoF-MSMG-PCNN) is proposed.

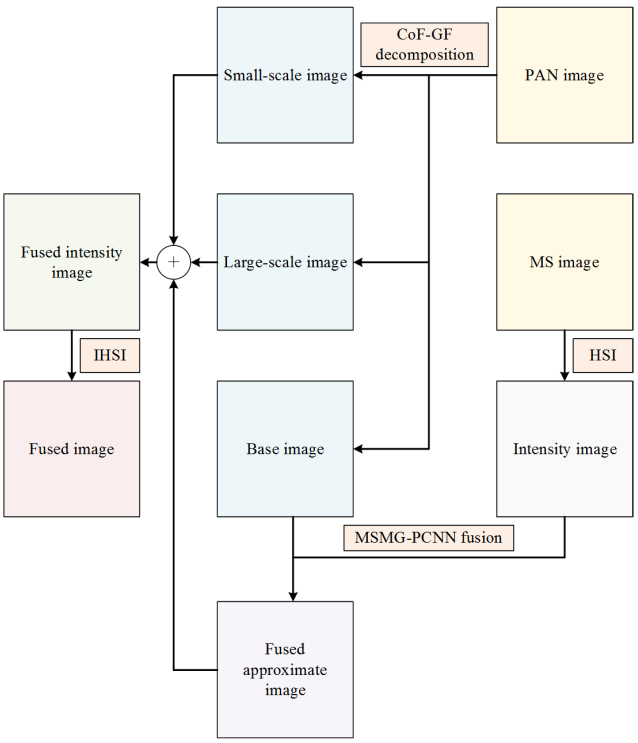

FIGURE 1. Framework of the CoF-MSMG-PCNN fusion method.

The framework of the proposed algorithm is shown in Fig. 1. It can be seen that the PAN image is decomposed

into small-scale image (S), large-scale image (L) and base image (B). Then the intensity image (I) of MS image and B is merged into a fused approximate image (FA) through MSMG-PCNN fusion rule. The fused intensity image (FI) is reconstructed by S, L and FA. Finally, the fused image is obtained by an inverse HSI transform.

In this section, the proposed algorithm, along with the required CoF and MSMG-PCNN theory, will be introduced.

A. CO-OCCURRENCE FILTERING

1) THEORY OF CoF

Co-occurrence filtering is an effective EPF which is proposed by Jevnisek and Avidan. Similar with the BF, pixel values which co-occur frequently will be smoothed, while the pixel values co-occur rarely will be preserved. The CoF is defined as

$$V_p = \frac{\sum_{q\in N(p)} w(p,q)\cdot U_q}{\sum_{q\in N(p)} w(p,q)} \tag{1}$$

where V_p and U_q are output and input, p and q are pixel indices. $w(p, q)$ is the weigh between input pixel p and output pixel q.

In GF, $w(p, q)$ is formed as

$$w(p,q) = \exp(-\frac{d(p,q)^2}{2\sigma_s^2})\cdot G_{\sigma_s}(p,q) \tag{2}$$

where $G_{\sigma_s}(p, q)$ deotes GF, $d(p, q)$ is the Euclidean distance between pixels p and q. And σ_s is the parameter which is related with the distribution of Gaussian function. In BF, $w(p, q)$ is defined as

$$w(p,q) = G_{\sigma_s}(p,q)\cdot \exp(-\frac{|I_p - I_q|^2}{2\sigma_r^2}) \tag{3}$$

where σ_r is a user designed coefficient.

In CoF, the GF is replaced with a normalized co-occurrence matrix. It takes the form of

$$w(p,q) = G_{\sigma_s}(p,q)\cdot M(I_p, I_q) \tag{4}$$

where M is a 256×256 matrix, which is computed by

$$M(m,n) = \frac{C(m,n)}{h(m)h(n)} \tag{5}$$

where M is obtained through a co-occurrence matrix $C(m, n)$. The values m and n denote the grayscale level, and $h(m)$ and $h(n)$ represent the corresponding frequency. C is defined as

$$C(m,n) = \sum_{p,q} \exp(-\frac{d(p,q)^2}{2\sigma^2})[I_p = m][I_q = n] \tag{6}$$

where σ is a designed coefficient, and the operation $[\cdot]$ means if the expression inside is true, the value will equal 1, otherwise the value equals 0.

Fig. 2 shows two examples of CoF. It can be seen that grass in (a) and the background in (b) are smoothed and removed, while the strong structures and edges are preserved.

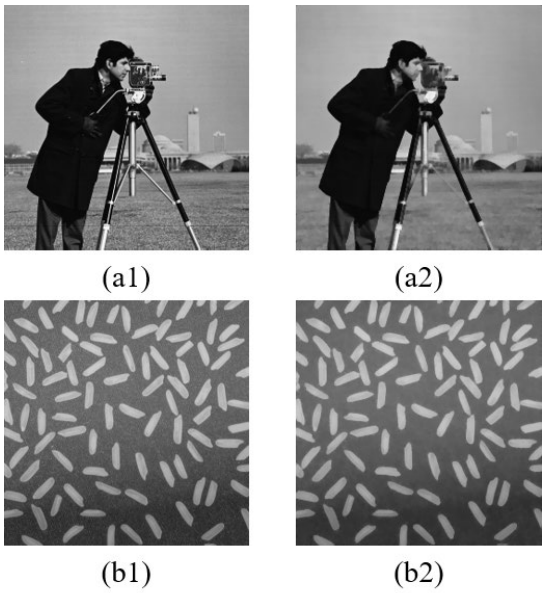

FIGURE 2. Two examples of CoF. (a1, b1) source images; (a2, b2) CoF results.

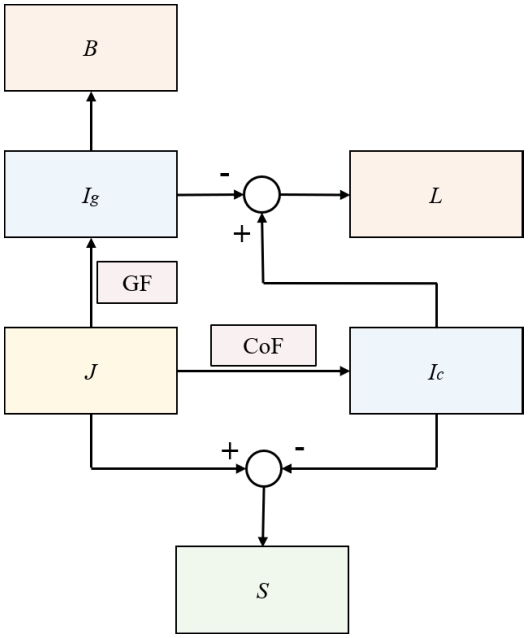

FIGURE 3. CoF and GF based image decomposition method.

2) CoF-BASED DECOMPOSITION METHOD

Since CoF preserves edges effectively, it can be used in image decomposition. In this paper, an image decomposition model based on CoF and GF is presented. An input image can be decomposed into three sub-images in different scales, through this decomposition method. As shown in Fig. 3, the process is divided into three steps: Firstly, the CoF and GF are used in the input image J to obtain filtered images I_c and I_g, respectively. Secondly, the small-scale image (S) is obtained by the difference between J and I_c, and the large-scale image (L) is also the differential result

between J and I_g. Finally, the base image (B) is represented by I_g. The decomposition process can be formulated as

$$I_g = GF(J, \sigma, \rho) \tag{7}$$
$$I_c = CoF(J, p) \tag{8}$$
$$S = J - I_c \tag{9}$$
$$L = I_c - I_g \tag{10}$$
$$B = I_g \tag{11}$$

where $GF(\cdot)$ and $CoF(\cdot)$ denote the Gaussian filtering and co-occurrence filtering operations, respectively. ρ and δ represent the radium size and variance of the GF. In this paper, if both the parameters are large, the fused image will appear unexpected block, and if they are small, the fused image will be not enough clear. Therefore, these two parameters are set to $\rho = 4, \delta = 10$. p represents the size of filter window. Similar with ρ and σ, p is set to 10.

B. MULTI-SCALE MORPHOLOGICAL GRADIENT DUAL-CHANNEL PCNN

1) MSMG OPERATOR

Multi-scale morphological gradient is an effective operator which can easily and well extract gradient information from an image. Since its superior characteristics, MSMG has been employed as a type of focus measure in multi-focus image fusion [23]. The specific details are described below.

Firstly, the multi-scale structuring element is defined as

$$SE_t = \underbrace{SE_1 \oplus SE_1 \oplus \cdots \oplus SE_1}_{t}, \quad t \in \{1, 2, \ldots, N\} \tag{12}$$

where SE_1 denotes a basic structure element, and t represents the number of scales. In this paper, the size of the structure element is set to 13, and t is set to 7.

Secondly, the gradient feature G_t can be represented by the morphological gradient operators from the image f

$$G_t(x, y) = f(x, y) \oplus SE_t - f(x, y) \ominus SE_t \tag{13}$$

where $\oplus$ and $\ominus$ denote the morphological dilation and erosion operators, respectively. (x, y) denotes the pixel coordinate.

Thirdly, MSMG is obtained by computing the weighted sum of gradients in all scales.

$$M(x, y) = \sum_{t=1}^{N} w_t \cdot G_t(x, y) \tag{14}$$

where w_t represents the weight of gradient in t-th scale, and it can be represented as

$$w_t = \frac{1}{2t + 1} \tag{15}$$

Fig. 4 shows the results of MSMG. It can be seen that the gradient information of the images have been well extracted.

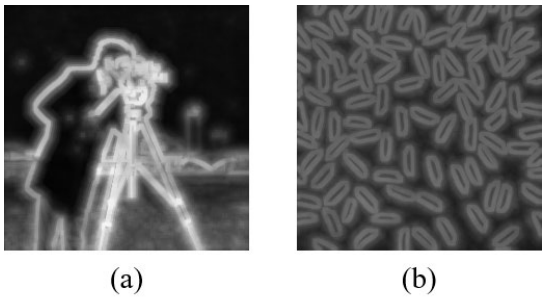

FIGURE 4. Results of MSMG. (a) MSMG of Fig. 2(a1); (b) MSMG of Fig. 2(b1).

2) CLASSICAL PCNN MODEL

As the third-generation artificial neural network, PCNN has achieved great success in image fusion field. A PCNN model often contains three parts: the receptive field, the modulation field and the pulse generator. The expressions of a simplified dual-channel PCNN model can be defined as

$$F_{ij}^1(k) = S_{ij}^1(k) \tag{16}$$
$$F_{ij}^2(k) = S_{ij}^2(k) \tag{17}$$
$$L_{ij}(k) = \begin{cases} 1, & \text{if } \sum_{r,t \in S} Y_{rt}(k-1) > 0; \\ 0, & \text{otherwise.} \end{cases} \tag{18}$$
$$U_{ij}(k) = \max\{F_{ij}^1(k)(1 + \beta_{ij}^1 L_{ij}(k)), F_{ij}^2(k)(1 + \beta_{ij}^2 L_{ij}(k))\} \tag{19}$$
$$Y_{ij}(k) = \begin{cases} 1, & \text{if } U_{ij}(k) \geq \theta_{ij}(k-1); \\ 0, & \text{otherwise.} \end{cases} \tag{20}$$
$$\theta_{ij}(k) = \theta_{ij}(k-1) - d_e + V_\theta Y_{ij}(k) \tag{21}$$
$$T_{ij} = \begin{cases} k, & \text{if } U_{ij}(k) \geq \theta_{ij}(k-1); \\ T_{ij}(k-1), & \text{otherwise.} \end{cases} \tag{22}$$

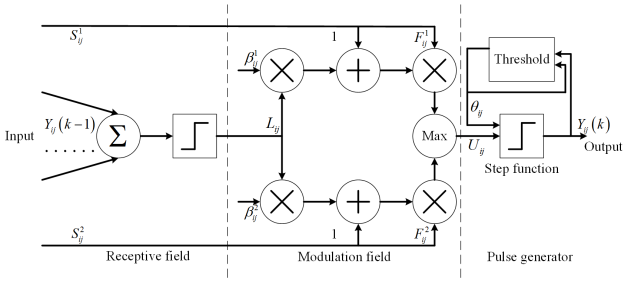

FIGURE 5. Classical PCNN model.

As is shown in Fig. 5, S_{ij}^1 and S_{ij}^2 denote the pixel value of two input images at the point (i, j) in this neural network; L_{ij} represents the linking parameter; β_{ij}^1 and β_{ij}^2 denote the linking strength; F_{ij}^1 and F_{ij}^2 represent the feedback of inputs. U_{ij} is the ouput of the dual-channel. θ_{ij} is the threshold of step function, d_e is the declining extent of the threshold, V_θ decides the threshold of the active neurons, and T_{ij} is the

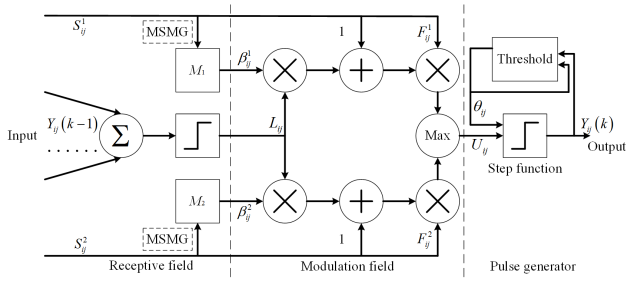

FIGURE 6. MSMG-PCNN model.

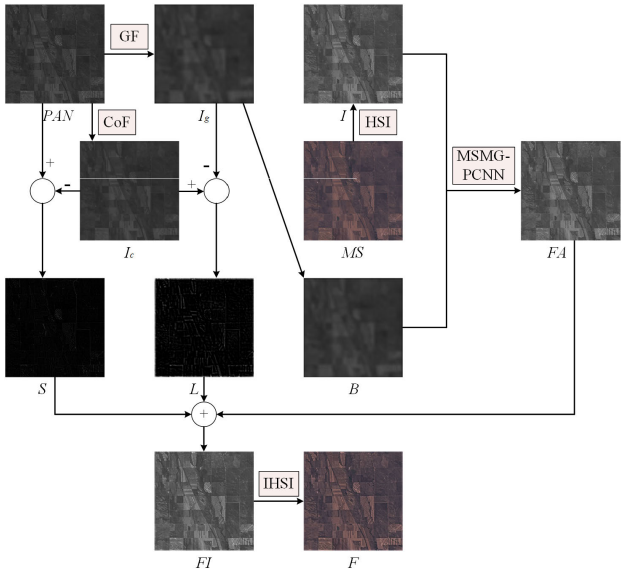

FIGURE 7. Diagram of the CoF-MSMG-PCNN algorithm.

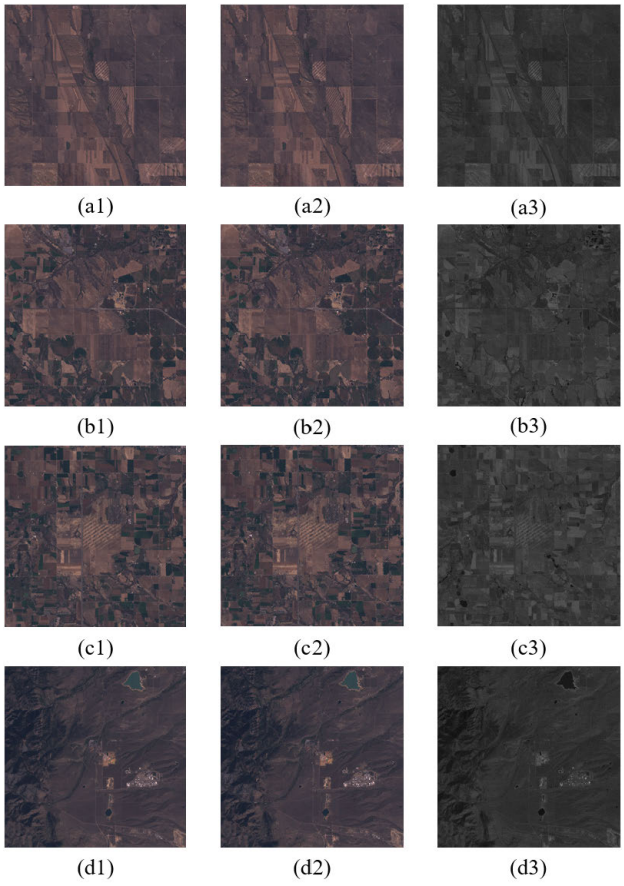

FIGURE 8. The display of four datasets. (a1, b1, c1, d1) 400 × 400 pixels MS images; (a2, b2, c2, d2) 200 × 200 pixels MS images; (a3,b3,c3,d3) 400 × 400 pixels PAN images.

parameter to determine the number of iterations. $Y_{ij}(k)$ is the k-th output of PCNN.

3) MSMG-PCNN MODEL

Although the PCNN model plays an important role in image fusion, it has a critical disadvantage: For an image, one pixel corresponds one neuron in PCNN. Once PCNN is alone used, it will be very difficult to find edge information. In this situation, the fusion result may produce local block and blurring. Since the MSMG operator directly affects the edge extraction in multiple scales, it is a good choice to use the MSMG-image modulate the PCNN model. In this paper, the MSMG operator is used to adjust the linking strength β_{ij}^1 and β_{ij}^2. The expression is denoted as

$$\beta_{ij}^1 = M_1 \tag{23}$$

$$\beta_{ij}^2 = M_2 \tag{24}$$

where M_1 and M_2 are the MSMG of input images I_1 and I_2, which can be computed by Formula (12). The schematic diagram of MSMG-PCNN model is shown in Fig. 6. Different from Fig. 5, the linking strengths β_{ij}^1 and β_{ij}^2 are modulated by MSMG operator.

C. CoF-MSMG-PCNN BASED FUSION METHOD

Since the MS and PAN images are acquired by different sensors, some positional deviation cannot be ignored. Image registration is required before fusion [24]. This paper focuses on the fusion algorithm. Therefore, the MS and PAN images used are all registered.

The fusion image can be divided into the following steps:

(1) The PAN image is decomposed into three sub-images S, L, B, through the CoF-based decomposition method. This step can be expressed by Formulas (7)-(11), where the input image is PAN.

(2) The MS image is transformed in the HSI domain by an HSI transformation. The intensity image I will be used in the next step.

(3) A fused approximate image FA is obtained through the MSMG-PCNN model for B and I. The two input images of the PCNN are B and I, and the output is FA.

(4) The fused intensity image FI is reconstructed by summation of S, L and FA.

(5) An inverse HSI transform is applied to the FI to obtain the fused image F.

It should be noted that MS and F are not only three bands. The reason for displaying RGB images is to look good in

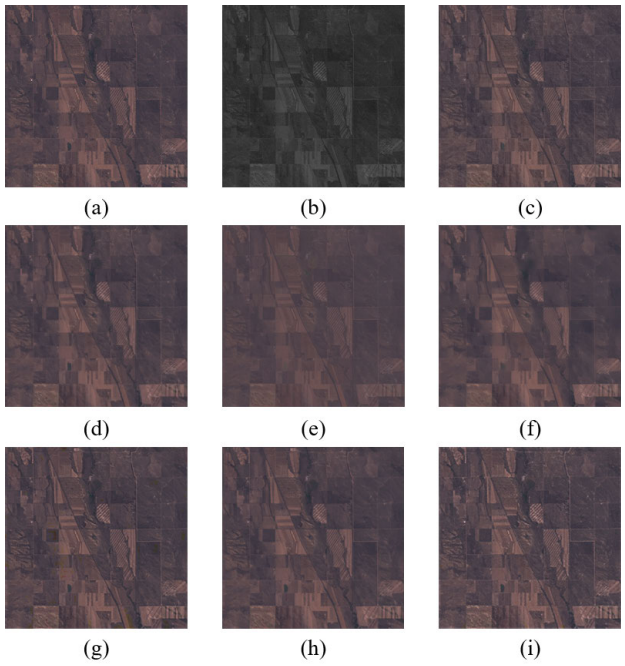

FIGURE 9. The first set of experiments. (a) MS image; (b) PAN image; (c) P + XS; (d) HSI; (e) PCA; (f) GIF; (g) CNN; (h) CAE; (i) Proposed.

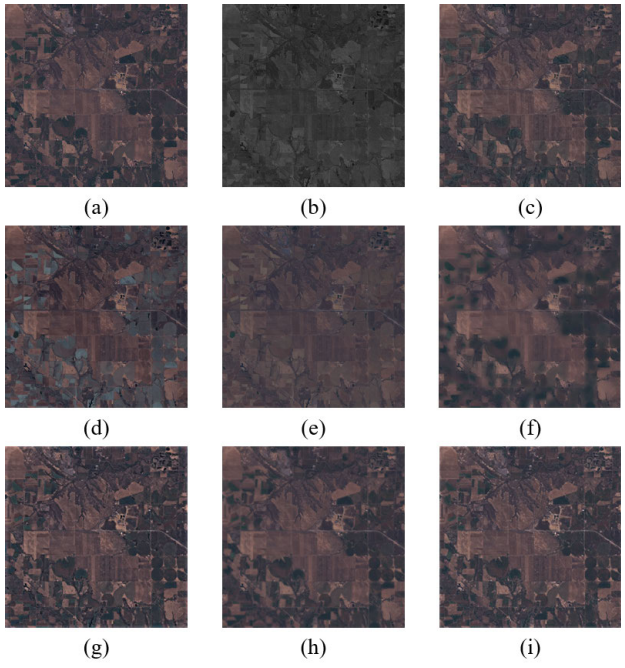

FIGURE 10. The second set of experiments. (a) MS image; (b) PAN image; (c) P + XS; (d) HSI; (e) PCA; (f) GIF; (g) CNN; (h) CAE; (i) Proposed.

visual effects. The diagram of the CoF-MSMG-PCNN based algorithm is shown in Fig. 7.

III. EXPERIMENTAL RESULTS

In order to evaluate the performance of the proposed algorithm, several sets of experiments are used to demonstrate. Meanwhile, several state-of-the-art algorithms, e.g. P + XS [25], HSI [6], PCA [7], guided image filtering (GIF) [26], convolutional neural network (CNN) [27], and convolutional autoencoder (CAE) [28] are used for qualitative and quantitative evaluation.

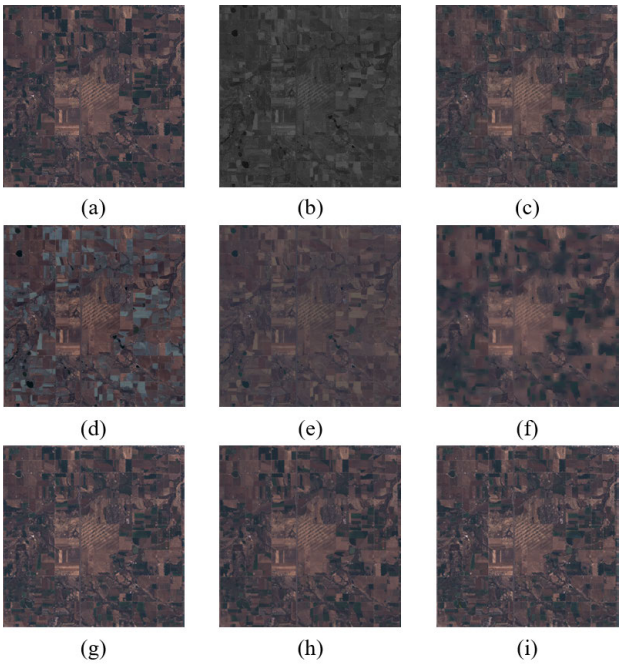

FIGURE 11. The third set of experiments. (a) MS image; (b) PAN image; (c) P + XS; (d) HSI; (e) PCA; (f) GIF; (g) CNN; (h) CAE; (i) Proposed.

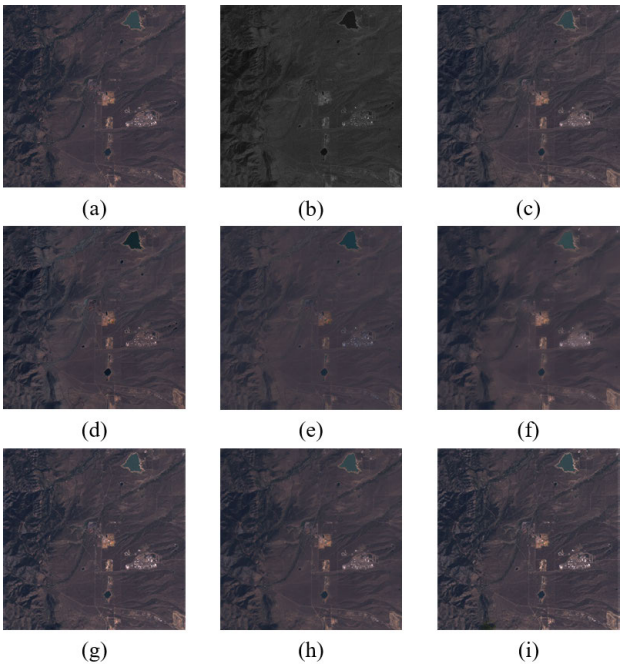

FIGURE 12. The fourth set of experiments. (a) MS image; (b) PAN image; (c) P + XS; (d) HSI; (e) PCA; (f) GIF; (g) CNN; (h) CAE; (i) Proposed.

A. DATASETS

A dataset containing 27 image pairs is used in this paper. These images are captured by Landsat Enhanced Thematic

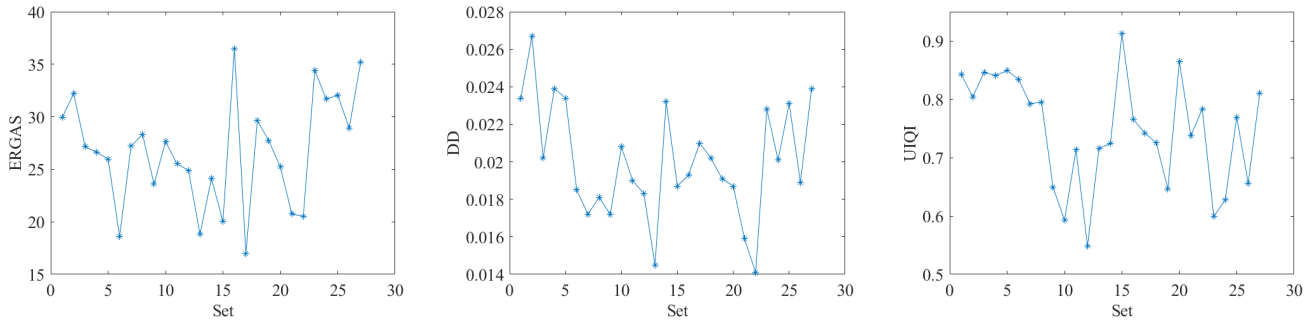

(a) ERGAS (b) DD (c) UIQI

FIGURE 13. Fusion results of all samples in the dataset. (a) ERGAS metrics; (b) DD metrics; (c) UIQI metrics.

Mapper Plus (LANDSAT 7 ETM+). They can be easily acquired from U.S. Geological service [29]. Meanwhile, the data can be also acquired from [30]. The images of the dataset have a size of 400 × 400 pixels, which works in 6 bands (Red, Green, Blue, Near-IR, Mid-IR, and shortwave-IR). The spatial resolution of MS images is 30 m, and 15 m for PAN image. Therefore, in this paper, the MS images are subsampled into 200 × 200 pixels. The MS image (200 × 200 pixels) and PAN image (400 × 400 pixels) are merged into an MS image with 400 × 400 pixels. And the 400 × 400 pixels source MS images will be used to as reference images. Fig. 8 is the display result of four randomly selected image pairs of the dataset, where (a1, b1, c1, d1) represent the size of 400 × 400 pixels MS images, (a2, b2, c2, d2) represent the size of 200 × 200 pixels MS images, and (a3, b3, c3, d3) represent the size of 400 × 400 pixels PAN images.

B. QUALITATIVE EVALUATION

Since human and machine decisions are heavily dependent on visual observation, the visual effect is a very important evaluation indicator. The visual effect largely determines the quality of the fusion results. Therefore, visual evaluation is essential for qualitative evaluation.

Figs. 9-12 show four sets of experiments. All the (a) and (b) are the source MS images and PAN images. (c)-(i) are the fused results of P + XS, HSI, PCA, GIF, CNN, CAE, and the proposed CoF-MSMG-PCNN methods, respectively. Every set of experiments will be described as follow.

Fig. 9 shows the first set of experiments with different methods. It can be seen that (e) and (f) are more blurred than the MS image. (c) and (d) have similar visual performance and they look sharper than the MS image. Moreover, (g), (h), and (i) appear to be enhanced over other images, which means that further quantitative evaluation is required.

Fig. 10 shows the second set of experiments. Spectral information distortion appears in (c) and (d). (e) loses some spectral information. (f) is blurred. (g), (h), and (i) have the same situation as Fig. 9.

Fig. 11 shows the third set of experiments. Similar to Fig. 10, spectral information distortion (c) and (g) are also blurred, (e) looks darker than the MS image. (g), (h), and (i) perform better than other methods and need further quantitative verification.

Fig. 12 shows the fourth set of experiments. Unlike previous experiments, all methods show similar results and similar visual quality. From the above four sets of experiments, quantitative evaluation is necessary.

It should be noted that experiments have been performed on the entire of the dataset. Figs. 9-12 are examples of comparison experiments. The fusion results of all samples and their statistical values will be given below.

C. QUANTITATIVE EVALUATION

Evaluating fusion effects based on visual effects alone is subjective. Moreover, the visual effects of the CNN and CAE methods are similar to the proposed method. Therefore, it still needs enough quantitative evaluation to demonstrate the proposed method is the best.

In this section, three metrics, the relative dimensionless global error in synthesis (ERGAS), the degree of distortion (DD), and the universal image quality index (UIQI) are employed to evaluate the fused results.

(1) ERGAS: The ERGAS measures the amount of spectral distortion. Given the fused image Z, and the reference image $\hat{Z}$, the ERGAS is defined as

$$\mathrm{ERGAS}(Z,\hat{Z}) = 100 \times \frac{s_P}{s_M}\sqrt{\frac{1}{m_\alpha}\sum_{\alpha=1}^{m_\alpha}\left(\frac{MSE(Z_\alpha,\hat{Z}_\alpha)}{\mu^2_{\hat{Z}_\alpha}}\right)} \quad (25)$$

where s_P/s_M is the ratio between the pixel sizes of the MS image and PAN image; Z_α and $\hat{Z}_\alpha$ represent the α-th bands of the fused image and the reference image; m_α is the number of MS bands; $MSE(\cdot)$ is the mean square error operator, and $\mu_{\hat{Z}_\alpha}$ is the mean of $\hat{Z}_\alpha$. The smaller is the ERGAS, the smaller is the error in the fused image.

(2) DD: As the name of DD, DD measures the degree of distortion between the fused image and the reference image,

TABLE 1. Quantitative evaluation of different methods.

Dataset	Index	AWLP	Brovey	IHS	P+XS	GIF	PCA	Proposed
1	ERGAS	25.0416	24.2034	27.5766	22.6624	18.7522	19.0347	**18.6223**
	DD	0.4317	0.3752	0.0888	0.0340	**0.0178**	0.0198	0.0185
	UIQI	0.7639	0.8182	0.7459	0.7971	0.8299	0.8216	**0.8339**
2	ERGAS	28.3726	44.4873	41.0244	**23.0877**	26.3195	24.9346	25.9786
	DD	0.6521	0.1200	0.1113	0.0566	0.0365	0.0261	**0.0234**
	UIQI	0.8260	0.4291	0.4210	0.8424	0.8468	0.8397	**0.8494**
3	ERGAS	29.0752	52.8293	47.3452	29.2526	26.6563	**25.9177**	26.6116
	DD	0.7567	0.1397	0.1237	0.0590	0.0312	0.0294	**0.0239**
	UIQI	0.7686	0.2539	0.2612	0.8305	0.8383	0.8334	**0.8404**
4	ERGAS	31.5069	35.4873	29.5563	29.2266	28.0308	27.6358	**27.1590**
	DD	0.4732	0.5160	0.0566	0.0379	0.0231	0.0302	**0.0202**
	UIQI	**0.8734**	0.7879	0.6948	0.8374	0.8474	0.8403	0.8462

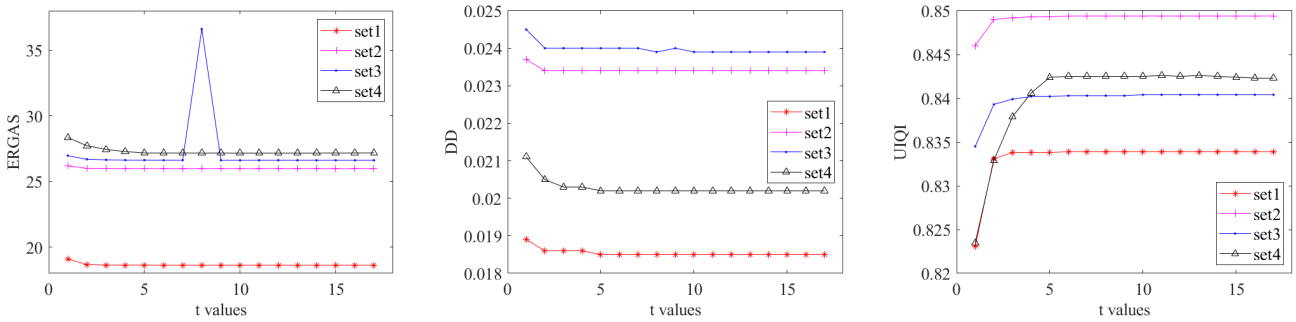

(a) t - ERGAS (b) t - DD (c) t - UIQI

FIGURE 14. The curves between t and three metrics. (a) t-ERGAS; (b) t-DD; (c) t-UIQI.

i.e. smaller DD means better fusion results. It is defined as

$$\mathrm{DD}(Z,\hat{Z}) = \frac{1}{s_M m_\alpha}\|\mathrm{vec}(Z) - \mathrm{vec}(\hat{Z})\|_1 \tag{26}$$

where $\mathrm{vec}(\cdot)$ represents the vectorization operator, and $\|\cdot\|_1$ is l_1 norm.

(3) UIQI: The UIQI is used to measure image distortion, correlation and contrast between the fused image and the reference image. The UIQI is defined as

$$\mathrm{UIQI}(Z,\hat{Z}) = \frac{4\sigma_{Z\hat{Z}}\cdot\mu_Z\cdot\mu_{\hat{Z}}}{(\sigma_Z^2+\sigma_{\hat{Z}}^2)(\mu_Z^2+\mu_{\hat{Z}}^2)} \tag{27}$$

where μ_Z and $\mu_{\hat{Z}}$ are mean of Z and $\hat{Z}$, σ_Z^2 and $\sigma_{\hat{Z}}^2$ are the corresponding variances, and $\sigma_{Z\hat{Z}}$ is the covariance between Z and $\hat{Z}$. The larger is the UIQI, the better is the fusion result.

The three metrics are obtained by Formulas (25)-(27). Table 1 shows the results with different methods. The best performance value of every line is displayed in bold. It can be seen that the proposed method works best in most of the cases. Therefore, our proposed method is better than other methods.

TABLE 2. The mean value and standard deviation of all the fusion results.

	ERGAS	DD	UIQI
Mean Value	26.6776	0.0200	0.7477
Standard Deviation	5.2061	0.0030	0.094

Moreover, the fusion results of all samples in the dataset is shown in Fig. 13. The mean value and standard deviation of all the fusion results are shown in Table 2.

IV. PARAMETER DISCUSSION

It should be noted that the value of parameter t in Formula (12) has a great influence on the fused result. It is because that t determines the gradient features information extracted from the input image. Fig. 14 shows the curves between t and three metrics ((a) t-ERGAS; (b) t-DD; (c) t-UIQI). It can be seen that all the three metrics will be converged with the increase of t. And when t values 11, most of the datasets will acquire the best performance. Therefore, t values 11 in this paper.

V. CONCLUSION

This paper proposes a novel remote sensing image fusion method. It is focused on the fusion of the MS image and PAN image. In this method, a very effective EPF called CoF is employed to decompose the PAN image, and a well-designed PCNN fusion strategy modulated by the MSMG operator is used to merge each band with small-scale PAN image. Finally, each fused bands are combined to obtain the fused image. Experimental results demonstrate that the proposed CoF-MSMG-PCNN method outperforms most methods.

ACKNOWLEDGMENT

The authors are grateful to the editors and the reviewers for their valuable comments and suggestions.

REFERENCES

[1] J. Guan, R. Lai, A. Xiong, Z. Liu, and L. Gu, "Fixed pattern noise reduction for infrared images based on cascade residual attention CNN," *Neurocomputing*, vol. 377, pp. 301–313, Feb. 2020.
[2] R. Lai, J. Guan, Y. Yang, and A. Xiong, "Spatiotemporal adaptive nonuniformity correction based on BTV regularization," *IEEE Access*, vol. 7, pp. 753–762, 2019.
[3] Y. Yang, L. Wu, S. Huang, W. Wan, and Y. Que, "Remote sensing image fusion based on adaptively weighted joint detail injection," *IEEE Access*, vol. 6, pp. 6849–6864, 2018.
[4] J. Wong, S. C. Liew, E. Wong, and Z. Lee, "Modeling the remote-sensing reflectance of highly turbid waters," *Appl. Opt.*, vol. 58, no. 10, pp. 2671–2677, Mar. 2019.
[5] S. Ji, S. Wei, and M. Lu, "Fully convolutional networks for multisource building extraction from an open aerial and satellite imagery data set," *IEEE Trans. Geosci. Remote Sens.*, vol. 57, no. 1, pp. 574–586, Jan. 2019.
[6] R. Masoudi and P. Kabiri, "New intensity-hue-saturation pan-sharpening method based on texture analysis and genetic algorithm-adaption," *J. Appl. Remote Sens.*, vol. 8, no. 1, May 2014, Art. no. 083640.
[7] J. Jelének, V. Kopačková, L. Koucká, and J. Mišurec, "Testing a modified PCA-based sharpening approach for image fusion," *Remote Sens.*, vol. 8, no. 10, p. 794, Sep. 2016.
[8] Y. Yang, L. Wu, S. Huang, J. Sun, W. Wan, and J. Wu, "Compensation details-based injection model for remote sensing image fusion," *IEEE Geosci. Remote Sens. Lett.*, vol. 15, no. 5, pp. 734–738, May 2018.
[9] C. A. Laben and B. V. Brower, "Process for enhancing the spatial resolution of multispectral imagery using pan-sharpening," U.S. Patent 6 011 875, Jan. 4, 2000.
[10] M. V. Joshi, L. Bruzzone, and S. Chaudhuri, "A model-based approach to multiresolution fusion in remotely sensed images," *IEEE Trans. Geosci. Remote Sens.*, vol. 44, no. 9, pp. 2549–2562, Sep. 2006.
[11] R. Lai, Y. Li, J. Guan, and A. Xiong, "Multi-scale visual attention deep convolutional neural network for multi-focus image fusion," *IEEE Access*, vol. 7, pp. 114385–114399, 2019.
[12] M. Ghahremani and H. Ghassemian, "Remote-sensing image fusion based on curvelets and ICA," *Int. J. Remote Sens.*, vol. 36, no. 16, pp. 4131–4143, Aug. 2015.
[13] M. R. Metwalli, A. H. Nasr, O. S. Faragallah, E.-S.-M. El-Rabaie, A. M. Abbas, S. A. Alshebeili, and F. E. A. El-Samie, "Efficient pan-sharpening of satellite images with the contourlet transform," *Int. J. Remote Sens.*, vol. 35, no. 5, pp. 1979–2002, Feb. 2014.
[14] Y. Yang, W. Wan, S. Huang, P. Lin, and Y. Que, "A novel pan-sharpening framework based on matting model and multiscale transform," *Remote Sens.*, vol. 9, no. 4, p. 391, Apr. 2017.
[15] J. Ma, Y. Ma, and C. Li, "Infrared and visible image fusion methods and applications: A survey," *Inf. Fusion*, vol. 45, pp. 153–178, Jan. 2019.
[16] Z. Zhou, B. Wang, S. Li, and M. Dong, "Perceptual fusion of infrared and visible images through a hybrid multi-scale decomposition with Gaussian and bilateral filters," *Inf. Fusion*, vol. 30, pp. 15–26, Jul. 2016.
[17] J. Ma, Z. Zhou, B. Wang, and H. Zong, "Infrared and visible image fusion based on visual saliency map and weighted least square optimization," *Infr. Phys. Technol.*, vol. 82, pp. 8–17, May 2017.
[18] W. Tan, H. Zhou, J. Song, H. Li, Y. Yu, and J. Du, "Infrared and visible image perceptive fusion through multi-level Gaussian curvature filtering image decomposition," *Appl. Opt.*, vol. 58, no. 12, pp. 3064–3073, Apr. 2019.
[19] R. J. Jevnisek and S. Avidan, "Co-occurrence filter," in *Proc. IEEE Conf. Comput. Vis. Pattern Recognit. (CVPR)*, Jul. 2017, pp. 3184–3192.
[20] Y. Yang, M. Yang, S. Huang, M. Ding, and J. Sun, "Robust sparse representation combined with adaptive PCNN for multifocus image fusion," *IEEE Access*, vol. 6, pp. 20138–20151, 2018.
[21] J. Qian, L. Yadong, D. Jindun, F. Xiaofei, and J. Xiuchen, "Image fusion method based on structure-based saliency map and FDST-PCNN framework," *IEEE Access*, vol. 7, pp. 83484–83494, 2019.
[22] W. Kong, L. Zhang, and Y. Lei, "Novel fusion method for visible light and infrared images based on NSST–SF–PCNN," *Infr. Phys. Technol.*, vol. 65, pp. 103–112, Jul. 2014.
[23] Y. Zhang, X. Bai, and T. Wang, "Boundary finding based multi-focus image fusion through multi-scale morphological focus-measure," *Inf. Fusion*, vol. 35, pp. 81–101, May 2017.
[24] J. Ma, J. Jiang, H. Zhou, J. Zhao, and X. Guo, "Guided locality preserving feature matching for remote sensing image registration," *IEEE Trans. Geosci. Remote Sens.*, vol. 56, no. 8, pp. 4435–4447, Aug. 2018.
[25] C. Ballester, V. Caselles, L. Igual, J. Verdera, and B. Rougé, "A variational model for P+XS image fusion," *Int. J. Comput. Vis.*, vol. 69, no. 1, pp. 43–58, Apr. 2006.
[26] Q. Li, X. Yang, W. Wu, K. Liu, and G. Jeon, "Pansharpening multispectral remote-sensing images with guided filter for monitoring impact of human behavior on environment," *Concurrency Comput., Pract. Exper.*, p. e5074, Nov. 2018.
[27] G. Scarpa, S. Vitale, and D. Cozzolino, "Target-adaptive CNN-based pansharpening," *IEEE Trans. Geosci. Remote Sens.*, vol. 56, no. 9, pp. 5443–5457, Sep. 2018.
[28] A. Azarang, H. E. Manoochehri, and N. Kehtarnavaz, "Convolutional autoencoder-based multispectral image fusion," *IEEE Access*, vol. 7, pp. 35673–35683, 2019.
[29] *US Gov*. Accessed: Oct. 24, 2019. [Online]. Available: https://earthexplorer.usgs.gov/
[30] *Dataset*. Accessed: Feb. 10, 2020. [Online]. Available: https://github.com/WilliamTitan/Pansharpening/tree/master/data/

WEI TAN received the B.S. degree in electronic science and technology from Xidian University, in 2014, where he is currently pursuing the Ph.D. degree. He is also a Guest Ph.D. Student with the University of Copenhagen, Denmark. His research interests include image processing, image fusion, pansharpening, and machine learning.

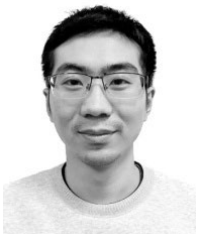

PEI XIANG received the B.S. degree in electrical engineering and automation from Qinghai University, in 2016. He is currently pursuing the Ph.D. degree with Xidian University. His research interests include hyperspectral image processing, remote sensing image analysis, pattern recognition, and object detection.

JIAJIA ZHANG received the B.S. degree in electronic science and technology from Xidian University, in 2017, where he is currently pursuing the Ph.D. degree. His research interests include image processing, image fusion, machine learning, and deep learning.

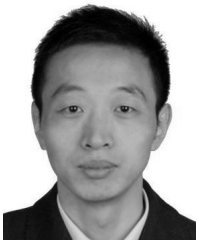

HUIXIN ZHOU received the B.S., M.S., and Ph.D. degrees in physics electronics from Xidian University, in 1996, 2002, and 2004, respectively. He is currently a Professor with the School of Physics and Optoelectronic Engineering, Xidian University. His research interests include optoelectronic imaging, image processing, object detection, hyperspectral imaging, and machine learning.

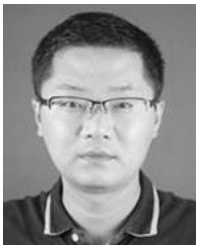

HANLIN QIN received the B.S., M.S., and Ph.D. degrees in physics electronics from Xidian University, in 2004, 2006, and 2010, respectively. He is currently an Associate Professor with the School of Physics and Optoelectronic Engineering, Xidian University. His research interests include optoelectronic imaging, object track, hyperspectral imaging, and deep learning.